Theory of modulational instability in Bragg gratings with quadratic nonlinearity

H. He,[1] Awdah Arraf,[1,2] C. Martijn de Sterke,[1] P. D. Drummond,[3] and Boris A. Malomed[4]
[1]*School of Physics, University of Sydney, Sydney 2006, New South Wales, Australia*
[2]*Australian Photonics Cooperative Research Center, 101 National Innovation Centre, Australian Technology Park, Eveleigh 1430, New South Wales, Australia*
[3]*Department of Physics, University of Queensland, Queensland 4072, Australia*
[4]*Department of Interdisciplinary Studies, Faculty of Engineering, Tel Aviv University, Tel Aviv 69978, Israel*
(Received 25 September 1998)

Modulational instability in optical Bragg gratings with a quadratic nonlinearity is studied. The electric field in such structures consists of forward and backward propagating components at the fundamental frequency and its second harmonic. Analytic continuous wave (CW) solutions are obtained, and the intricate complexity of their stability, due to the large number of equations and number of free parameters, is revealed. The stability boundaries are rich in structures and often cannot be described by a simple relationship. In most cases, the CW solutions are unstable. However, stable regions are found in the nonlinear Schrödinger equation limit, and also when the grating strength for the second harmonic is stronger than that of the first harmonic. Stable CW solutions usually require a low intensity. The analysis is confirmed by directly simulating the governing equations. The stable regions found have possible applications in second-harmonic generation and dark solitons, while the unstable regions may be useful in the generation of ultrafast pulse trains at relatively low intensities. [S1063-651X(99)03005-6]

PACS number(s): 42.65.Tg

I. INTRODUCTION

Optical parametric systems have attracted considerable attention in recent years. This is partly through obvious applications to second-harmonic and subharmonic generation, and also because they support a large range of multidimensional solitary wave solutions or ''simultons,'' of both topological and nontopological nature [1–16]. The major difference between a simulton and a Kerr type soliton is the source of nonlinearity. The nonlinear effect in forming a simulton is rooted in the parametric process in which two waves of different frequencies interact strongly through the $\chi^{(2)}$ nonlinearity, while that of a Kerr soliton is due to the nonlinear refractive index. The different mechanism of providing nonlinearity in parametric systems offers two key advantages over Kerr systems. First, the parametric nonlinear effect can be much stronger than the Kerr effect. Thus a much lower input power is required to launch solitary waves. Second, solitary waves in more than one dimension do not usually exist in a nonsaturating Kerr system, but are supported in parametric systems.

These two advantages have a potential impact on both the theory and applications of optical solitons. For example, in quantum optics, a strong nonlinear effect translates to a large effective binding energy between photons. It was shown theoretically that a quantum simulton consisting of only two photons can exist [17]. Combining the low power requirements and multidimensionality of simultons, a compact ultrafast all-optical switching device which is not phase sensitive was recently proposed [18].

Much progress has been made on simulton experiments. The existence of spatial simultons were experimentally confirmed in 1995 [19]. Recently, temporal simultons have also been observed [20]. The reason that temporal simultons were observed later is that material dispersion is normally small, which means that the formation distance of a simulton is often longer than the length of available materials. This difficulty can be overcome by mixing diffraction into dispersion by tilting the wave front [20], or by ''writing'' a Bragg grating into the material, to create a ''gap simulton.'' The reported experiment takes the first approach [20]. However, the main focus of this paper is the second approach, which not only offers the opportunity of engineering the dispersion, but also supports solitons with new physics. For example, gap simultons can propagate at a speed much lower than the speed of light (even zero speed). Using Bragg gratings to create strong dispersion is well known in Kerr systems [21], but applying this technique to parametric systems has only been studied recently [22–25]. We term the parametric system with Bragg gratings a ''parametric band-gap system'' [22,23]. Encouragingly, theoretical studies have proven the existence of bright simultons in a parametric band-gap system not only in one dimension [22–25] but also in two- and three dimensions [22,23]. In one dimension, dark simultons are also found [22–25].

In this paper we study the modulational instability (MI) of continuous electromagnetic waves in the the parametric band-gap system, for a number of reasons. The first of these is that MI in the closely related problem of a grating with a Kerr nonlinearity has proven interesting, and has led to potential applications of such structures as tunable pulse generators [26]. Second, the absence of MI is a necessary condition for the stable copropagation of second-harmonic and subharmonic fields, and hence for the stability of dark simultons. Since these applications of our work are outside the scope of this paper, our main objective here is to solve the one dimensional coupled parametric band-gap equations for continuous wave (CW) solutions and to determine their stability.

Modulational instability of a parametric system without gratings has been studied previously Refs. [14,27,28]. Full

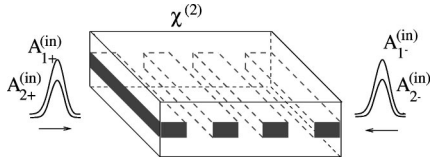

FIG. 1. Schematic of the double band gap system, combining refractive-index modulation with a quadratic nonlinearity.

analytical results were reported in [28]. This system is described by a pair of coupled equations, whose modulational instability is a function of only two parameters: the ratio of dispersions at the fundamental and second harmonic and the phase mismatch between the two waves. MI in a Kerr system with gratings was studied [29,30], also leading to a set of two coupled equations, but for the forward and backward propagating modes. The stability of parametric simultons in the Kerr limit has also been studied [38]. In contrast to this work, a parametric band-gap system is described by four coupled equations whose modulation instability is a function of five parameters, that will be discussed below. The doubling of the number of equation and the addition of extra free parameters greatly increase the level of complexity of the MI problem in the new system. Even solving the equations for CW solutions is not trivial. Nevertheless, the modulational instability of a band-gap parametric system is treated here by combining both analytical and numerical approaches. To test the results of modulational instability analysis, the full coupled equations are simulated directly using two different methods [31,32].

The paper is organized as follows: we introduce the coupled parametric band-gap equations in Sec. II. The four coupled equations are then solved for CW solutions in Sec. III. Details of MI analysis are given in Sec. IV. Physical interpretations using approximate techniques, together with numerical results, are given in Sec. V. Finally, methods of numerical simulations and results are presented in Sec. VI.

II. COUPLED PARAMETRIC BAND-GAP EQUATIONS

A parametric band-gap system is indicated schematically in Fig. 1, which shows a nonlinear waveguide with modulated refractive index, and two sets of counterpropagating fields. We consider a degenerate parametric process. Two waves of different frequencies are involved: the first harmonic or the fundamental harmonic (FH) and the second harmonic (SH). We denote the carrier frequencies of the FH and SH by ω_1 and ω_2, respectively, where $\omega_2=2\omega_1$. Each has two possible propagation directions; we just consider one-dimensional waveguides without additional transverse effects. Devices of this type have been fabricated in experiments for efficient second-harmonic generation [33]. For simplicity, we take the waveguide to be infinitely long. We thus do not need to consider boundary conditions, which play important roles in bistability and other effects. Of course, though any actual system is finite, the results of such analysis still give valuable insight [37]. In practice one may only need to introduce one of the four fields as inputs to obtain a steady state, as either fundamental field can generate photons in the other three modes.

The system is similar to the doubly resonant optical parametric oscillation (OPO) cavity system, which has been extensively studied in theory and experiment [34,35]. In the case considered here, however, there is a continuum of longitudinal modes, which must be treated using a set of coupled parametric band-gap equations. The detailed derivation of the equations in the shallow grating limit can be found in Ref. [22]. A more rigorous derivation has extended the results to deep gratings [36]. Here we consider shallow gratings only.

For a quasimonochromatic electric field inside Bragg gratings, we can write the solutions to Maxwell's equation for fields around ω_1,ω_2 as [22]

$$\mathbf{E}=\sum_{j=1,2}\sum_{\pm}\mathbf{e}_j\mathcal{A}_{j\pm}(z,t)e^{\pm ijk_1z-i\omega_jt}+\text{c.c.}, \tag{2.1}$$

where $\mathbf{e}_j$ are unit vectors indicating polarization directions, the sign $\pm$ represents right or left propagation, and jk_1 is the effective wave number of the corresponding carrier field. Assuming type-I phase matching, the Bragg grating structure is given as $\epsilon_j(z)=\overline{\epsilon_j}[1+\Delta_j(z)]$, where $\overline{\epsilon_j}$ is the spatial average of $\epsilon_j(z)$ and $j=1$ and 2. Note that $\overline{\epsilon_{1,2}}$ (and $\Delta_{1,2}$) differ due to material dispersion. We consider $\Delta_j(z)$ to be the small parameter here because of the shallow grating assumption, and the results are expanded in terms of a small parameter $\Delta\simeq\Delta_j(z)$. Here the permittivity $\epsilon_j(z)$ is a periodic function with a period of d. We can expand $\epsilon_j(z)$ in a Fourier series, with

$$\Delta_j(z)=\sum_l\Delta_{jl}\exp(2ilk_1z)+\text{c.c.}, \tag{2.2}$$

where Δ_{jl} are in general complex coefficients, and $k_1=\pi/d$. Note that we have chosen the carrier wavenumber of the FH to be the same as that of the grating. The carrier frequency is $\omega_1=k_1/\sqrt{\mu_0\overline{\epsilon_1}}$, and the carrier wave number of the SH is $k_2=2\sqrt{\mu_0\overline{\epsilon_2}}\omega_1$. We define $\delta k=k_2-2k_1\ll k_1$, the phase mismatch due to material dispersion.

With the above definitions, a parametric band-gap system is described by the following coupled equations [22]:

$$\begin{aligned}
&i\left[\frac{1}{v_g^{(1)}}\frac{\partial}{\partial t}+\frac{\partial}{\partial z}\right]\mathcal{A}_{1+}+\kappa_1\mathcal{A}_{1-}+\chi_E\mathcal{A}_{1+}^*\mathcal{A}_{2+}=0,\\
&i\left[\frac{1}{v_g^{(1)}}\frac{\partial}{\partial t}-\frac{\partial}{\partial z}\right]\mathcal{A}_{1-}+\kappa_1^*\mathcal{A}_{1+}+\chi_E\mathcal{A}_{1-}^*\mathcal{A}_{2-}=0,\\
&i\left[\frac{1}{v_g^{(2)}}\frac{\partial}{\partial t}+\frac{\partial}{\partial z}\right]\mathcal{A}_{2+}+\delta k\mathcal{A}_{2+}+\kappa_2\mathcal{A}_{2-}+\chi_E\mathcal{A}_{1+}^2=0,\\
&i\left[\frac{1}{v_g^{(2)}}\frac{\partial}{\partial t}-\frac{\partial}{\partial z}\right]\mathcal{A}_{2-}+\delta k\mathcal{A}_{2-}+\kappa_2^*\mathcal{A}_{2+}+\chi_E\mathcal{A}_{1-}^2=0,
\end{aligned} \tag{2.3}$$

where $\chi_E=\omega_1^2\tilde{\chi}^{(2)}/(k_1c^2)$, $\tilde{\chi}^{(2\mathbf{e}_1^*\cdot\chi^{(2)}\cdot\mathbf{e}_1^*\mathbf{e}_2=\mathbf{e}_2^*\cdot\chi^{(2)}\cdot\mathbf{e}_1\mathbf{e}_1}$, and $\kappa_j=jk_1\Delta_{jj}/2$. To simplify the equations, we can always choose the phases of $\mathbf{e}_j$ so that χ_E is real. We neglect group velocity dispersion of the medium, as this is usually much smaller than the grating dispersion. However, we have in-

cluded the difference in material group velocities between the two carriers, as this is not always negligible.

To reduce the number of free parameters, it is convenient to normalize Eqs. (2.3). Generally speaking, the phase difference between both gratings can be arbitrary. This means that both κ_1 and κ_2 are complex. Here we only consider cases in which the gratings are either in phase or out of phase. Thus both κ_1 and κ_2 can be made real by choosing the origin of the coordinate correctly. In fact, we chose the origin such that κ_1 is real and positive. With these choices, we introduce the relations

$$\begin{aligned} \mathcal{A}_{1\pm} &= \frac{\kappa_1}{\chi_E}\sqrt{\frac{v_g^{(1)}}{v_g^{(2)}}}V_{1\pm}, \\ \mathcal{A}_{2\pm} &= \frac{\kappa_1}{\chi_E}V_{2\pm}, \\ \xi &= \kappa_1 z, \\ \tau &= v_g^{(1)}\kappa_1 t. \end{aligned} \tag{2.4}$$

Substituting these definitions into Eqs. (2.3) gives the normalized equations

$$\begin{aligned} i\left(\frac{\partial}{\partial\tau}+\frac{\partial}{\partial\xi}\right)V_{1+}+V_{1-}+V_{1+}^{*}V_{2+}&=0, \\ i\left(\frac{\partial}{\partial\tau}-\frac{\partial}{\partial\xi}\right)V_{1-}+V_{1+}+V_{1-}^{*}V_{2-}&=0, \\ i\left(\frac{\partial}{\partial\tau}+r_v\frac{\partial}{\partial\xi}\right)V_{2+}+\rho V_{2+}+\gamma V_{2-}+V_{1+}^{2}&=0, \\ i\left(\frac{\partial}{\partial\tau}-r_v\frac{\partial}{\partial\xi}\right)V_{2-}+\rho V_{2-}+\gamma V_{2+}+V_{1-}^{2}&=0, \end{aligned} \tag{2.5}$$

where $r_v=v_g^{(2)}/v_g^{(1)}$ is the ratio of group velocity of the FH and the SH, $\rho=r_v\delta k/\kappa_1$ is a normalized phase mismatch, and $\gamma=r_v\kappa_2/\kappa_1$ is the ratio of the grating strengths at SH and FH. The number of free parameters of our equations hence reduces to three.

III. CW SOLUTIONS

CW solutions to Eqs. (2.5) can be written in the general form

$$V_{j\pm}=a_{j\pm}e^{-ij\Omega\tau+ijQ\xi}, \quad j=1,2, \tag{3.1}$$

where $a_{j\pm}$ are complex amplitudes, Ω is the frequency, and Q is the wave number of the CW solution. Substituting the above ansatz into Eqs. (2.5), we have

$$\begin{aligned} a_{1+}(\Omega-Q)+a_{1+}^{*}a_{2+}+a_{1-}&=0, \\ a_{1-}(\Omega+Q)+a_{1-}^{*}a_{2-}+a_{1+}&=0, \\ (2\Omega-2r_vQ+\rho)a_{2+}+\gamma a_{2-}+a_{1+}^{2}&=0, \\ (2\Omega+2r_vQ+\rho)a_{2-}+\gamma a_{2+}+a_{1-}^{2}&=0. \end{aligned} \tag{3.2}$$

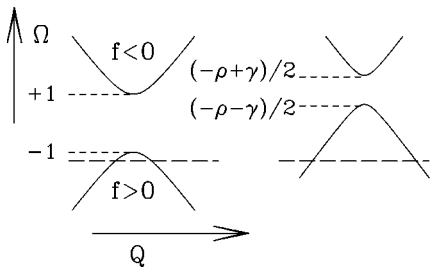

FIG. 2. Band gaps at the FH (left-hand side) and SH (right-hand side). Shown is the local frequency Ω vs the local wave number Q at the two gaps. In our normalized parameters, the fundamental gap has a width of 2, whereas the second harmonic gap has a width of $2|\gamma|$ and an offset of $-\rho$. The horizontal long-dashed lines indicate a fundamental frequency (left-hand side), and its second harmonic (right-hand side). Note that γ is taken to be positive.

From Eq. (2.5), one notices that if $a_{j\pm}$ are solutions, then $a_{j\pm}e^{ij\theta}$, where θ is a constant phase factor, are also solutions. This symmetry indicates that we can always choose θ such that one of $a_{j\pm}$ is real. Taking a_{1+} to be real together with Eq. (3.2), one can show that a_{1-} is also real unless a very specific relationship among a_{1+},γ,Ω,Q and the real part of a_{1-} is satisfied. Thus, for a given set of parameters, it can only occur for a specified intensity. We do not consider such nongeneric behavior here. Once we have taken $a_{1\pm}$ to be real, it is trivial to deduce from Eq. (3.2) that $a_{2\pm}$ are also real.

To understand the physical meaning of the various parameters, we consider the linear version of Eq. (3.2). That is Eq. (3.2) without the nonlinear terms. Two uncoupled linear dispersion relationships can be obtained from the linear equation. For clarity, the two dispersion relationships are shown in Fig. 2 for $r_v=1$. It shows the local frequency Ω versus the local wave number Q at the fundamental gap (left-hand side), and the second-harmonic gap (right-hand side). In our normalized parameters, the fundamental gap has a width of two units, whereas the second harmonic gap has a width of $2|\gamma|$, and has an offset of $-\rho$. The horizontal long-dashed lines indicate a fundamental frequency (left-hand side), and its second harmonic (right-hand side).

To obtain nonlinear CW solutions, we still need to solve the full Eq. (3.2). CW solutions are usually classified into two categories: (1) degenerate solutions and (2) nondegenerate solutions. We discuss each type of solution separately.

A. Degenerate solutions

Degenerate CW solutions are solutions that have vanishing components. In practical terms, we can either allow the second-harmonic field or the subharmonic field to vanish. However, no stable solution that is nontrivial results when the second-harmonic field vanishes. In order to see this, we notice that if we assume that $a_{2\pm}=0$, then we can deduce that $a_{1\pm}=0$ immediately from Eq. (3.2). This gives the vacuum state

$$a_{j\pm}=0. \tag{3.3}$$

If we assume that $a_{1\pm}=0$ and $a_{2\pm}\neq 0$, we find that only the last two of Eqs. (3.2) need to be satisfied. In other words, for a vanishing subharmonic field, the solutions to Maxwell's

equations only involve the usual linear behavior in a Bragg grating. There are solutions both above and below band gap, and any of the usual band-gap CW modes can be excited. This allows us to choose any two of Ω, Q, a_{2+}, and a_{2-} as free parameters. If we choose Q and a_{2-}, we obtain the relationships

$$a_{1\pm}=0,$$
$$\Omega=\frac{\mp\sqrt{4\,Q^2r^2+\gamma^2}-\rho}{2}, \tag{3.4}$$
$$a_{2+}=\frac{a_{2-}(-2\,Q\,r\pm\sqrt{4\,Q^2r^2+\gamma^2})}{\gamma}.$$

In this solution, only the second harmonic exists—some of these degenerate solutions can be unstable against spontaneous down-conversion. These stability properties will be analyzed in Sec. III B.

B. Nondegenerate CW solutions

To obtain the general nondegenerate CW solutions in analytic form, we use the parametrizations introduced by de Sterke [29]:

$$a_{1+}=\frac{a}{\sqrt{f^2+1}},$$
$$a_{1-}=\frac{af}{\sqrt{f^2+1}}. \tag{3.5}$$

These equations imply that $a_{1+}^2+a_{1-}^2=a^2$ and $a_{1-}/a_{1+}=f$. Using Eqs. (3.5) and rearranging the last two equations of Eqs. (3.2), we have

$$a_{2+}=-f+Q-\Omega,$$
$$a_{2-}=-f^{-1}-Q-\Omega. \tag{3.6}$$

The meaning of f can be understood as determining the position of the FH component of the CW solution. For example, taking $f=\pm1$ and substituting Eq. (3.6) into Eq. (3.2), we find that

$$2Q(2fr_v+2\Omega r-\gamma+\rho+2\Omega)=0.$$

Therefore, $f=\pm1$ corresponds to $Q=0$, indicating that the FH components of the matching CW solutions are at the edges of the fundamental band gap. Since κ_1 was taken to be positive, in the linear limit $f<1$ indicates an anomalous dispersion and tuning above the band gap, whereas $f>1$ gives normal dispersion below the band gap, as shown in Fig. 2. A detailed discussion of the f parameter can be found in Ref. [29]. A new feature in the double-band-gap case treated here is that the fundamental and second-harmonic band gaps can have different widths, indicated by γ, as well as different locations, indicated by ρ (see Fig. 1).

The most general CW solutions can be found in closed form and are discussed in Appendix A. However, when $Q=0$, and thus $f=\pm1$, the CW solutions take a simpler form.

TABLE I. Summary of CW solutions to the parametric band-gap system. Shown here is one degenerate solution and a nondegenerate solution with $f^2=1$. The vacuum state and more general CW solutions with $f^2\neq1$ are not listed for simplicity.

Mode	Degenerate solutions	Nondegenerate solutions
a_{1+}	0	$\pm\sqrt{(\Omega+f)(2\Omega+\gamma+\rho)}$
a_{1-}	0	fa_{1+}
a_{2+}	$a_{2-}(-2\,Q\,r+\sqrt{4\,Q^2r^2+\gamma^2})/\gamma$	$-\Omega-f$
a_{2-}	arbitrary	$-\Omega-f$

We therefore consider the case $f=\pm1$ separately. For clarity, both degenerate and nondegenerate CW solutions are summarized in Table I.

$f=\pm1$

Using an effective mass approximation (EMA) [22,23], we have proven previously that the parametric band-gap equations (2.3), which apply to second order nonlinear systems without a grating, have soliton solutions; key aspects of this work are reviewed in Appendix B. The idea is that solutions to the parametric equations (B1), can be transformed approximately to solutions to the parametric band-gap equations. Such a transformation is general and not limited just to solitonlike solutions, provided that the EMA is valid. The requirement of the EMA to be valid is that $Q\ll1$. The EMA transformation gives exact CW solutions to the parametric band-gap equations when $Q=0$, i.e., when $f=\pm1$. Note that the EMA can also give approximate CW solutions for small Q. However, we do not discuss such cases here.

CW solutions to parametric equations (B1) can easily be obtained [13,28]. The EMA transformation between the parametric equations and the parametric bandgap equation is given as

$$V_{1+}=g_1V_1\mathrm{sgn}(\kappa_1),$$
$$V_{1-}=-g_1V_1s_1,$$
$$V_{2+}=g_2V_2s_1, \tag{3.7}$$
$$V_{2-}=g_2V_2s_1,$$

where $V_1=\pm\sqrt{2\alpha}$, $V_2=\mathrm{sgn}(s_1h)$, and $\alpha=|\kappa_2v_g^{(1)}/(\kappa_1v_g^{(2)})|\times|2-(2s_1|\kappa_1|v_1+\kappa_2v_2+\delta kv_2)/h|$, $h=-v_1\kappa_1(\Omega+f)$, $g_1=\sqrt{|\kappa_1v_2/(2\kappa_2v_1)|}|h|e^{i\Omega\tau}/(\kappa_1v_1)$, and $g_2=|h|e^{2i\Omega\tau}/(\kappa_1v_1)$.

Simplifying the above relationships, one arrives at

$$a_{1+}=\pm\sqrt{(\Omega+f)(2\Omega+\gamma+\rho)},$$
$$a_{2\pm}=-\Omega-f, \tag{3.8}$$

and $a_{1-}=a_{1+}f$ according to Eq. (3.5). The above solutions are the same as the solutions obtained by solving Eqs. (3.2) directly.

IV. MODULATION INSTABILITY ANALYSIS

Following the standard procedure [37], we now add small perturbations to the CW solutions and study their evolution. We thus set

$$V_{j\pm}=[a_{j\pm}+\delta_{j\pm}(\xi,\tau)]e^{-ij\Omega\tau+ijQ\xi}. \tag{4.1}$$

Substituting this into Eq. (2.5) and neglecting terms involving $\delta_{j\pm}^2$ gives

$$\begin{aligned}
&i\left(\frac{\partial}{\partial\tau}+\frac{\partial}{\partial\xi}\right)\delta_{1+}+\delta_{1+}(\Omega-Q)+\delta_{1-}+\delta_{1+}^{*}a_{2+}+a_{1+}\delta_{2+}\\
&\quad=0,\\
&i\left(\frac{\partial}{\partial\tau}-\frac{\partial}{\partial\xi}\right)\delta_{1-}+\delta_{1-}(\Omega+Q)+\delta_{1+}+\delta_{1-}^{*}a_{2-}+a_{1-}\delta_{2-}\\
&\quad=0,\\
&i\left(\frac{\partial}{\partial\tau}+r_v\frac{\partial}{\partial\xi}\right)\delta_{2+}+\delta_{2+}(2\Omega-2r_vQ+\rho)+\gamma\delta_{2-}\\
&\qquad+2a_{1+}\delta_{1+}=0,\\
&i\left(\frac{\partial}{\partial\tau}-r_v\frac{\partial}{\partial\xi}\right)\delta_{2-}+\delta_{2-}(2\Omega+2r_vQ+\rho)+\gamma\delta_{2+}\\
&\qquad+2a_{1-}\delta_{1-}=0,
\end{aligned} \tag{4.2}$$

Below, we discuss the modulational instability of degenerate CW solutions and nondegenerate CW solutions separately.

A. Degenerate case

We start with the degenerate case for which $a_{1\pm}=0$, so that Eqs. (4.2) decouple. Therefore, we introduce

$$\begin{aligned}
\delta_{1+}&=g_1(\tau)e^{iq\xi}+g_3^{*}(\tau)e^{-iq\xi},\\
\delta_{1-}&=g_2(\tau)e^{iq\xi}+g_4^{*}(\tau)e^{-iq\xi}.
\end{aligned} \tag{4.3}$$

Substituting the above equations into Eq. (4.2) and collecting same exponential terms gives

$$\begin{aligned}
&i\frac{d}{d\tau}g_1+(\Omega-Q-q)g_1+g_2+a_{2+}g_3=0,\\
&i\frac{d}{d\tau}g_2+(\Omega+Q+q)g_2+g_1+a_{2-}g_4=0,\\
&i\frac{d}{d\tau}g_3-(\Omega-Q+q)g_3-g_4-a_{2+}g_1=0,\\
&i\frac{d}{d\tau}g_4-(\Omega+Q-q)g_4-g_3-a_{2-}g_2=0.
\end{aligned} \tag{4.4}$$

The above ordinary differential equations have fundamental solutions which are linear combinations of terms that are of the form

$$g_j(\tau)\propto e^{i\omega\tau}, \tag{4.5}$$

where the ω are the eigenvalues of the matrix

$$\begin{pmatrix}
\Omega-Q-q & 1 & a_{2+} & 0\\
1 & \Omega+Q+q & 0 & a_{2-}\\
-a_{2+} & 0 & -\Omega+Q-q & -1\\
0 & -a_{2-} & -1 & -\Omega-Q+q
\end{pmatrix}. \tag{4.6}$$

This matrix is real and nonsymmetric, so its eigenvalues are real or appear in complex conjugate pairs. CW solutions are stable only if all eigenvalues are real. For brevity, we only consider $Q=0$. This corresponds physically to a second-harmonic band-gap mode either at the top edge or the bottom edge of the second-harmonic band gap.

Substituting $Q=0$ into Eqs. (3.4) divides the CW solutions into two different classes: $a_{2+}=a_{2-}$, and $a_{2+}=-a_{2-}$. In analogy to the parameter f from Eq. (3.5), we can also introduce a parameter f_2 which is the ratio of a_{2+} and a_{2-} [cf. Eq. (3.5)]. Together with the sign of κ_2, f_2 tells us the position of the SH component of the solution. If $\kappa_2>0$, $a_{2+}=a_{2-}$ corresponds to the lower edge of the band-gap since $f_2=1$, whereas $a_{2+}=-a_{2-}$ corresponds to the upper edge of the band-gap since $f_2=-1$ [29].

If $a_{2+}=a_{2-}$, the eigenvalues of the matrix can be written in the form

$$\omega=\pm\sqrt{R\pm2\sqrt{\Delta}}, \tag{4.7}$$

where $R=1+\Omega^2+q^2-a_{2-}^2$, and $\Delta=(q^2+1)\Omega^2-a_{2-}^2q^2$. To have a stable CW solution, ω must be real for all q. It is thus necessary that $\Delta>0$. Thus, $\Omega^2>a_{2-}^2$. Next we notice that $R-2\sqrt{\Delta}>0$ at large q^2. However, if this quantity changes sign at any positive value of q^2, then the CW solution must be unstable. Solving $R-2\sqrt{\Delta}=0$ for q^2 gives two solutions q_0, where $q_0^2=\Omega^2-(a_{2-}\pm1)^2$. The condition $q_0^2<0$ must also be satisfied for a stable CW solution, giving $\Omega^2<(a_{2-}-1)^2$. Combining this with the previous requirement, $\Omega^2>a_{2-}^2$, we find that the amplitude of a_2 cannot be too large, and we must satisfy the overall requirement that

$$a_{2-}^2<\min(1/4,\Omega^2). \tag{4.8}$$

Therefore, CW solutions of this type are always unstable if $\Omega=0$, and otherwise have a limited range of stability up to a critical value of a_{2-}^2.

In order to understand the physics behind this, we notice that the down-conversion process requires both energy conservation and a symmetry requirement that the cross section is nonzero. Although this is rather complex at high intensities, it becomes relatively simple to understand at low intensities. If we refer to the Fig. 2, we notice that a symmetric mode must couple to two subharmonic modes of the same symmetry (either both above or both below the band gap). This is impossible if the second harmonic is excited at low amplitudes in a region whose energy is located *between* the upper and lower band gaps of the subharmonic. Thus, we expect stable behavior at low intensities for any value of Ω satisfying $\Omega^2<1$, which is precisely the result given by the eigenvalue analysis at low intensity.

The eigenvalues of the matrix for the second case, $a_{2+}=-a_{2-}$, can be written in the same form,

$$\omega=\pm\sqrt{R\pm\sqrt{\Delta}}, \tag{4.9}$$

where $R=1+\Omega^2+q^2-a_{2-}^2$, and $\Delta=(q^2+1)(\Omega^2-a_{2-}^2)$. Note that Δ now takes a different form. Again, to guarantee $\Delta>0$, we must have $\Omega^2>a_{2-}^2$. Solving $R-\sqrt{\Delta}=0$ for q^2 gives only one solution. This indicates that $R-\sqrt{\Delta}$ is either greater or smaller than 0 regardless the value of q as long as $\Omega^2>a_{2-}^2$ is satisfied. Taking $q=0$, we find $R-\sqrt{\Delta}=[(\Omega^2-a_{2-}^2)^{1/2}-1]^2$. Therefore, CW solutions of this type are stable when $\Omega^2>a_{2-}^2$.

The physical reason for this result is that an antisymmetric second-harmonic mode can only couple to two subharmonic modes of the opposite symmetry (one above and one below the band gap). If the second harmonic is excited at low amplitudes, this is only energy-conserving in a region almost in the center of the band gap of the subharmonic, which is just the opposite of the previous case. Thus, we expect stable behavior at low intensities for any value of $\Omega\neq 0$, which is, again, precisely the result given by the eigenvalue analysis at low intensity.

B. Nondegenerate case

In this general case, we take the perturbations to be of the forms [37]

$$\begin{aligned}
\delta_{1+}&=g_1(\tau)e^{iq\xi}+g_5^*(\tau)e^{-iq\xi},\\
\delta_{1-}&=g_2(\tau)e^{iq\xi}+g_6^*(\tau)e^{-iq\xi},\\
\delta_{2+}&=g_3(\tau)e^{iq\xi}+g_7^*(\tau)e^{-iq\xi},\\
\delta_{2-}&=g_4(\tau)e^{iq\xi}+g_8^*(\tau)e^{-iq\xi}.
\end{aligned} \tag{4.10}$$

Similar to Sec. IV A, we have $g_j(\tau)\propto e^{i\omega\tau}$. The eigenvalues ω are determined by the matrix

$$\mathbf{A}=\begin{pmatrix}
A_{11} & 1 & a_{1+} & 0 & a_{2+} & 0 & 0 & 0\\
1 & A_{22} & 0 & a_{1-} & 0 & a_{2-} & 0 & 0\\
2a_{1+} & 0 & A_{33} & \gamma & 0 & 0 & 0 & 0\\
0 & 2a_{1-} & \gamma & A_{44} & 0 & 0 & 0 & 0\\
-a_{2+} & 0 & 0 & 0 & A_{55} & -1 & -a_{1+} & 0\\
0 & -a_{2-} & 0 & 0 & -1 & A_{66} & 0 & -a_{1-}\\
0 & 0 & 0 & 0 & -2a_{1+} & 0 & A_{77} & -\gamma\\
0 & 0 & 0 & 0 & 0 & -2a_{1-} & -\gamma & A_{88}
\end{pmatrix}, \tag{4.11}$$

where $A_{11}=-q-Q+\Omega$, $A_{22}=q+Q+\Omega$, $A_{33}=-qr_v-2Qr_v+\rho+2\Omega$, $A_{44}=qr_v+2Qr_v+\rho+2\Omega$, $A_{55}=-q+Q-\Omega$, $A_{66}=q-Q-\Omega$, $A_{77}=-qr_v+2Qr_v-\rho-2\Omega$, and $A_{88}=qr_v-2Qr_v-\rho-2\Omega$. We note that changing the signs of f, γ, Ω, and ρ, and swapping the sign in the solution of the quadratic Eq. (A2), effectively changing the sign of Q, the determinant of the 8×8 matrix (4.11), is unchanged. We therefore only need to consider cases with positive γ.

As in Sec. IV A, a stable CW solution requires all eigenvalues of the above matrix to be real. Eigenvalues of the this 8×8 matrix are not usually available in simple analytic form. We hence obtain the eigenvalues numerically. We use a FORTRAN77 subroutine, DGEEV from the LINPACK, to evaluate the eigenvalues. To determine the stability of a given CW solution, we compute the instability growth rate $\mathrm{Im}(\omega)$ by varying q from 0 to 20 with a step size of 0.01. If the maximum of $\mathrm{Im}(\omega)$ at this stage is smaller than 10^{-8}, we further increase the range of q and reduce the step size and repeat the calculation. We consider a CW solution to be stable if the maximum of $\mathrm{Im}(\omega)$ is smaller than 10^{-8}.

The main difficulty with proceeding further is that there are five degrees of freedom in choosing the parameters r_v, f, γ, ρ, and Ω. Nevertheless, we can narrow our search by considering the physical significance of the five parameters: (1) r_v, the ratio of material group velocities at the FH and the SH. For most materials, this ratio is around unity. Three values, $r_v=0.5$, 1.0, and 2.0, were chosen to represent a large range of possible situations. (2) f gives the position of a CW solution with respect to the fundamental band-gap. Typical values of f are $f=\pm 0.1$, ± 0.5, and ± 1.0. Note that f and $1/f$ are equivalent, the only difference being the direction of propagation [29]. (3) γ represents the relative strengths of the gratings at the FH and the SH. The

values $\gamma=0.1$, 0.5, 1, 2, and 10 cover a large range of situations (recall that $\pm\gamma$ lead to the same results). (4) ρ is the phase mismatch between the FH and the SH due to material dispersion. (5) Ω relates to the intensity,

$$a_{1+}^2+a_{1-}^2+a_{2-}^2+a_{2+}^2, \tag{4.12}$$

of a CW solution. In experiments, ρ and Ω can be varied continuously, and there are no typical values. We therefore treat them as ''free,'' and scan ρ, and Ω space for MI at given values of r_v, f, and γ.

V. RESULTS AND INTERPRETATION

As the number of variables is large, it is difficult to obtain much physical intuition from the equations as they stand, even though they do give an exact solution for the stability properties of the CW solutions to the parametric band-gap problem. We know that only those combinations of CW amplitudes that satisfy the steady-state equations, and have stable eigenvalues, are able to exist as stable, translationally invariant, coupled fields inside the grating. To obtain more physical insight, it is useful to consider various limits that allow the problem to become more analytically tractable, and more closely comparable to similar band-gap problems that have been treated previously. In particular, we consider the nonlinear Schrödinger (NLS) equation limit, where the problem essentially reduces to the usual nonlinear refractive index case, as one limit that has been extensively studied previously. Another limit of interest, is the case when $f=\pm1$, so that the Bragg-grating polariton modes behave essentially identically to low-velocity massive particles.

A. Nonlinear Schrödinger equation limit

In the NLS limit, the SH can be adiabatically eliminated, leaving just the lower-frequency field. This means that the problem reduces to the usual problem of a Bragg grating with a nonlinear refractive index. A further simplification, discussed below, is possible in some cases. This reduces the entire problem to a single nonlinear Schrödinger equation for a single polariton mode of the lower-frequency Bragg grating. The approximation is somewhat analogous to the reduction of a relativistic nonlinear field theory (which contains particle and antiparticles), to a simpler nonrelativistic field theory. As in the relativistic case, the approximate theory contains only slowly moving particles of one type, in the appropriate physical regime.

This limit requires two conditions: low intensity

$$a_{1+}^2+a_{1-}^2+a_{2-}^2+a_{2+}^2\ll1$$

and large phase mismatch. The second condition implies

$$\gamma\ll\rho,$$

so that the linear coupling terms in the last two of Eqs. (2.5) can be neglected. Thus these equations can be written approximately as $V_{2\pm}=-V_{1\pm}^2/\rho$ [4], and the first two of Eqs. (2.5) that remain reduce to evolution equations similar to those for a grating with a Kerr nonlinearity. In turn, these equations reduce to the NLS equation in the low-intensity limit [29,38,39]. Thus the four coupled parametric band-gap equations are now approximated by the NLS equation,

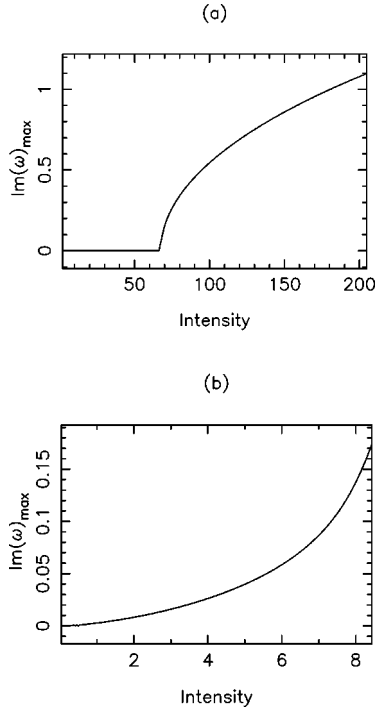

FIG. 3. Maximum instability growth rate vs intensity at positive phase mismatch ρ, and negative f. According to the NLS equation, the CW solution is now stable. Parameters used are $r_v=1$, $f=-0.8$, $\gamma=0$, (a) $\rho=100$ corresponding to large phase mismatch, and (b) $\rho=10$ corresponding to medium phase mismatch.

$$i\frac{\partial u}{\partial\tau}-\frac{1}{2}\Omega''\frac{\partial^2u}{\partial\xi^2}+A|u|^2u=0, \tag{5.1}$$

where $\Omega''=-8/(f+f^{-1})^3$ is the dispersion, $A=-(f^2+f^{-2})/[\rho(f+f^{-1})^2]$ is the effective nonlinear coefficient, and $|u|^2=a_{1+}^2+a_{1-}^2=a^2$. The dispersion is normal when $f>0$ and anomalous when $f<0$. The sign of the nonlinearity is determined by ρ. MI of the NLS has been solved previously [37]. It is well known that stable CW solutions require normal dispersion and positive nonlinearity or anomalous dispersion and negative nonlinearity ($f\rho<0$). CW solutions are unstable otherwise ($f\rho>0$). More accurately, the stability is determined by the eigenvalues

$$\omega=\pm\tfrac{1}{2}|\Omega''|q\sqrt{q^2-q_0^2}, \tag{5.2}$$

where $q_0^2=(f^2+f^{-2})(f+f^{-1})a^2/(2\rho)$. The solutions are real for all q if $f\rho<0$, so the CW solutions can be stable against small perturbations for small a^2. By contrast, the solutions are imaginary if $f\rho>0$ and $|q|<q_0$, and CW solutions are thus unstable.

To compare the above predictions with results obtained from solving the full matrix [Eq. (4.11)], we vary the value of ρ while keeping a relatively small. The intensity is varied by changing Ω. We thus plot the instability growth rate versus intensity for each given set of parameters. For the stable cases $f\rho<0$, we choose $f=-0.8$, $r_v=1$, and $\gamma=0$. Two different cases are discussed, $\rho=100$ and 10. The results are

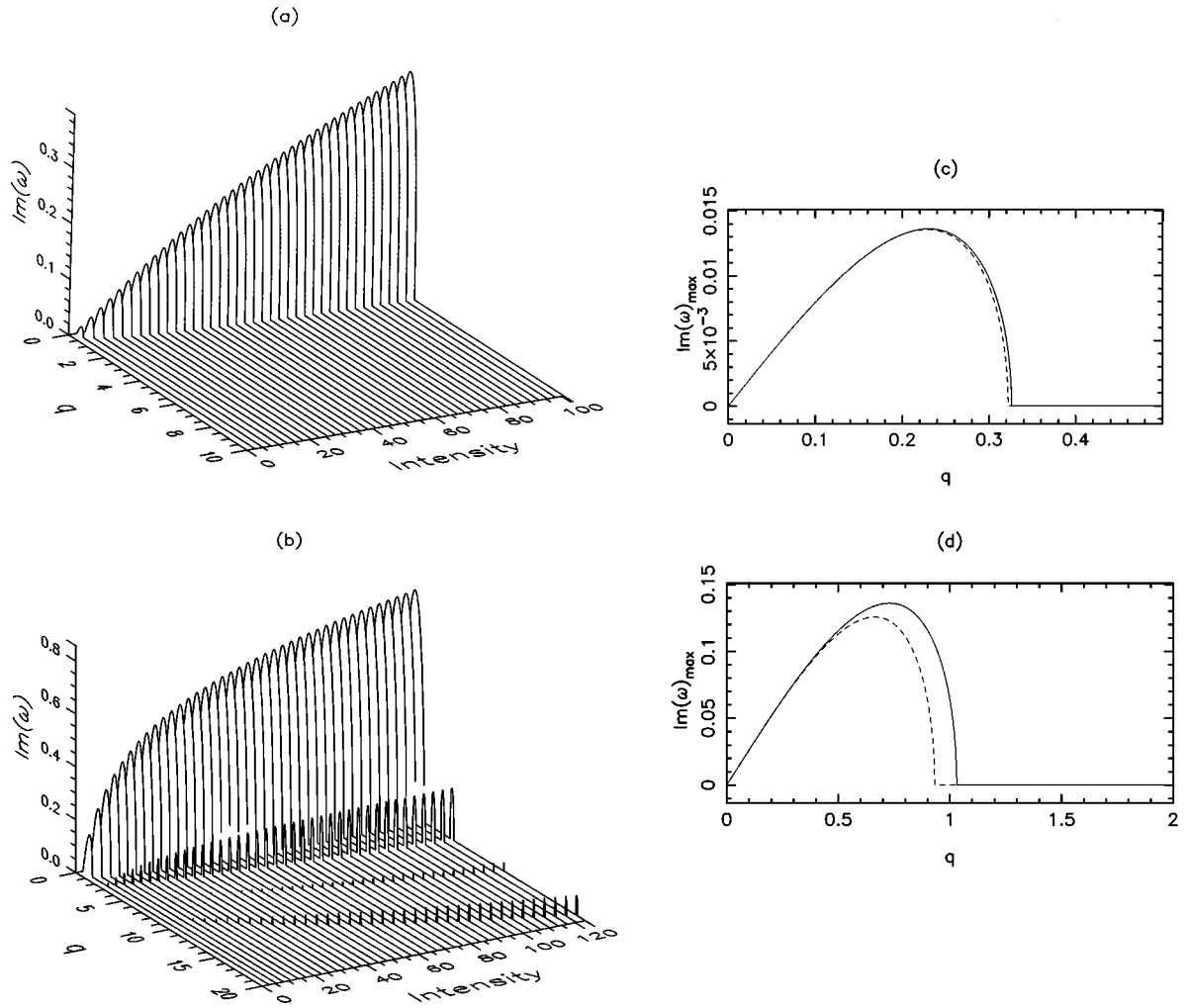

FIG. 4. Instability growth rate vs intensity and perturbation wave number q at positive phase mismatch and positive f. According to the NLS equation, the CW solution is now unstable. Parameters used are $r_v=1, f=0.5$, and $\gamma=0$ and the following: (a) and (c) $\rho=100$ corresponding to large phase mismatch; (b) and (d) $\rho=10$ corresponding to medium phase mismatch. (c) and (d) $a=2$. Solid lines follow from Eq. (5.2), and dashed lines from Eq. (4.11).

shown in Figs. 3(a) and 3(b), respectively, in which the maximum instability growth rates versus intensity are plotted. These figures show that CW solutions are stable when the intensity is low. In Fig. 3(a), $\rho=100$, so that the equation is well within the NLS limit. This figure shows a stable region for the intensity smaller than 70 consistent with the MI analysis of the NLS equation. For intensities larger than 70, the full system is unstable. This cannot be accounted for by the NLS because the intensity is too high for the NLS to be valid. By contrast, in Fig. 3(b) ($\rho=10$), we observe unstable regions even at low intensities. The instability growth rate grows dramatically as the intensity increases. This cannot be explained by the NLS treatment since ρ is not sufficiently large.

To illustrate the unstable cases for which $f\rho>0$, we take $f=0.5$, $r_v=1$, and $\gamma=0$. The instability growth rates versus q and intensity are shown in Figs. 4(a) and 4(b), corresponding to $\rho=100$ and 10 respectively. The topology of the instability demonstrates the familiar ''butterfly'' patterns in the MI of the NLS when ρ is large, as shown in Fig. 4(a). In Fig. 4(b), we find a new pattern emerging beside the main feature of the NLS type MI. This is not surprising since the CW solution is moving out of the NLS limit. The new instability is relatively small and, therefore, the maximum instability is still determined by the NLS type instability. In Figs. 4(c) and 4(d), we plot the instability growth rate predicted by Eq. (5.2) using a solid line, and that predicted by the 8×8 matrix [Eq. (4.11)] using a dashed line. We take $a=2$ for these two figures, leaving other parameters unchanged. The figures show again that the NLS analysis agrees with the full matrix very well at a large phase mismatch. The difference between both results become apparent only for small phase mismatch, as expected.

B. Case: $f^2=1$

In the EMA limit of $f=\pm1$, the problem reduces to a study of coupled, nonrelativistic massive particles. This follows since the dispersion relation for each field is then identical to that of the Schrödinger equation, for polariton modes near the upper and lower band-gap boundaries. This case gives a simplified two-mode equation (for two coupled polariton modes), that is equivalent to the known problem of modulational stability of coupled FH and SH waves in a uniform nonlinear waveguide, as described by the one-dimensional parametric equation. This reduction is quite

analogous to the well-known reduction of the two-mode (coupled) nonlinear Schrödinger equation to the single-mode nonlinear Schrödinger equation, already described.

As discussed in Sec. III B, CW solutions for this case can be obtained by the EMA transformation. One might expect that the MI in the case can also be obtained from the EMA transformation. However, the EMA is not valid for large wave numbers. Therefore, stability obtained from solving the full 8×8 matrix may contradict those from the EMA. Nonetheless, we find that consideration of the EMA mode couplings helps explain some of the physics of the full analysis. Thus the EMA theory (in certain cases) allows the reduction of the present problem to the well-understood case of a uniform quadratically nonlinear medium. In this simpler case, a necessary (but not sufficient) condition for stability is that the dispersion of the two modes have opposite signs [12,27,28]. Hence we do not expect stability if the dominant coupling is between linear eigenmodes that are both above or both below their respective band gaps. This follows because the effective dispersion is anomalous above a band gap, and normal below a band gap. Thus, from Fig. 2, we can see that, unless the excitation frequency is near a band gap, both the coupled modes have the same sign of dispersion. This is not likely to give stable behavior.

In the present case, with $f^2=1$, the FH is excited just at the edge of its band gap (the bottom edge if $f=1$, and the top edge if $f=-1$). Therefore, this argument would indicate modulationally unstable behavior if the corresponding SH mode is excited below or above the band gap, respectively. However, the excitation frequency of the SH relative to its band gap depends on both the size of the band gap ($|\gamma|$), and the relative phase mismatch parameter (ρ). For example, from Fig. 2, it is clear that the top of the bands are aligned in frequency if $\rho-|\gamma|=-2$, which should be unstable for an $f=-1$ excitation. Similarly, the bottom of the bands align if $\rho+|\gamma|=2$, which gives an instability for an $f=1$ excitation.

The EMA analysis also shows that the couplings of the modes depends on the sign of γ. If $\gamma>0$, the preferential coupling is to SH modes *below* the band gap. If $\gamma<0$, the preferential coupling is to SH modes *above* the band gap. Thus we can expect different types of instability depending on the sign of γ. The sign of γ depends on the relative Fourier coefficients of the refractive-index modulation, and hence on the details of the fabrication of the gratings.

Since we took the CW solutions to be real, we deduce from Eq. (3.8) that they must satisfy either $(\Omega+f)>0,(2\Omega+\gamma+\rho)>0$, or $(\Omega+f)<0,(2\Omega+\gamma+\rho)<0$. Apart from the signs of f and γ, these two cases lead to the same results; there is a symmetry obtained from simultaneously reversing the signs of f, γ, Ω, and ρ, consistent with our general finding in the paragraph below Eq. (4.11). We therefore only show results for the first situation. We vary Ω from $-f$ or $-(\gamma+\rho)/2$, whichever is larger, up to 10 and ρ from -10 up to 10. Thus a three-dimensional plot of maximum instability growth rate is obtained for each set of r_v and γ. Generally most CW solutions are unstable. Nevertheless, a few stable solutions are found when the intensity is low, when ρ is around zero and γ is large. This small stable region shrinks as γ decreases. CW solutions are unstable for high intensity and large ρ.

A series of plots is given in Figs. 5 for $f=-1$ (above the fundamental band gap) and 6 for $f=1$ (below the fundamental bandgap). We take $r_v=1$ in both cases for definiteness, and $\gamma=10,4$, and 1, as representative examples, as shown in (a), (b), and (c), respectively. The strongest coupling between the quasimodes is here expected to be to the SH modes *below* the bandgap, since γ is positive, as mentioned above.

In Fig. 5(a), $\gamma=10$ and $f=-1$, the stable area is the largest of all figures. This is not completely unexpected, since the fundamental excitation is just above the band gap, giving anomalous dispersion, whereas the nonlinear coupling is predominantly to SH modes (below) the band gap, which have normal dispersion. Therefore, the quasi modes that are coupled have opposite signs of dispersion—a necessary condition for stability in the EMA limit. Note that the sign of the phase mismatch clearly is important as well.

When $\gamma=2$ [Fig. 5(b)], we notice that the previous single large stable region at $\gamma=10$ separates into a number of much smaller stable regions. At $\gamma=1$ [Fig. 5(c)], the size of all stable regions shrink even further to disappear. Only tiny stable regions still survive at $\rho\approx-1$. We note that the stable region at large ρ and small intensity in Fig. 5(c) corresponds to the NLS limit.

The parameters in Fig. 6 are identical to those in Fig. 5 except that $f=1$. Thus $\gamma=10$, 2, and 1 in Figs. 6(a), 6(b), and 6(c), respectively. Note that the stable regions in these figures are almost entirely isolated from the vacuum state; a CW solution's intensity thus needs to exceed a threshold to be stable. We also find that compared to Fig. 6(a), the extent of stable regions reduce dramatically in Fig. 6(b) and vanish in Fig. 6(c). Again, the NLS limit can be seen at the largest values of the phase mismatch ρ in Fig. 6(c). For $\gamma<1$, stable regions are found mainly at large ρ, which again corresponds to the NLS limit. However, we do not show these results here. We note that the stable region in Fig. 6(a) has a low-intensity boundary at $\rho=12$. According to Fig. 2, and with the parameters chosen, the lower edge of the FH gap now lines up with the upper edge of the SH gap. However, according to the EMA theory, the effective nonlinear coupling between the FH and SH vanishes in this case [22,24,25], so that, within this approximation, the system behaves as if it were linear. Hence the EMA appears to be applicable here, and the stability at $\rho=12$ is not surprising. A similar argument applies to $\gamma=2$ in Fig. 6(b), where the stable region occurs at the low-intensity value of $\rho=6$. We cannot draw similar conclusions at $\gamma=1$ since the stable region in Fig. 6(c) does not extend to low intensities. We also note that this argument does not appear to apply to Figs. 5.

Our results indicate that a relative large grating strength for the SH [large γ; see Eq. (2.5)] tends to stabilize the CW solutions. We also studied the effect of group velocity mismatch r_v. Varying r_v, we repeated the calculations discussed above. The results show that r_v also plays an important role in determining the MI. When we take $r_v=0.5$, the stable area expands at $\gamma=10$, whereas if $r_v=2$, the stable area shrinks. Taking $\gamma=1$, we find that small deviations of r_v from unity reduce stable regions. However, we do not show these results here.

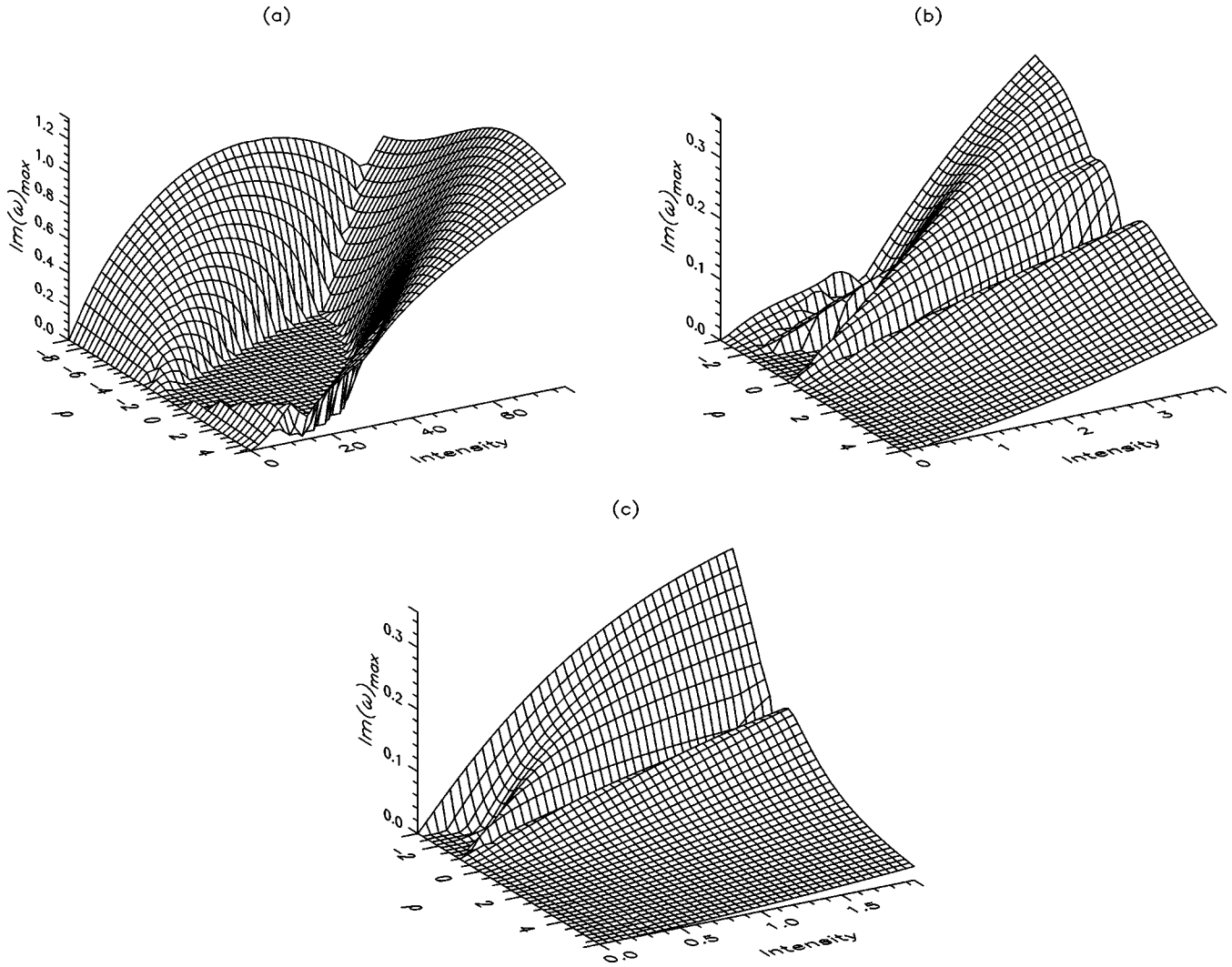

FIG. 5. Maximum instability for different grating strength ratios γ and negative f. Plotted here is growth rate vs phase mismatch ρ and intensity. Parameters used are $r_v=1$, $f=-1$, (a) $\gamma=10$, (b) $\gamma=2$, and (c) $\gamma=1$. Note that all axes are scaled differently.

C. Case: $f^2 \neq 1$

Here there is no physically similar model which is available to help interpret the results, and we are forced to rely solely on numerical solutions of the eigenvalue problem. We scan parameter values, thus taking a similar strategy to the previous section. Gradually moving $|f|$ away from 1, we compute the maximum instability in the Ω, ρ space for each different value of γ. In general, we find that CW solutions can be stable only at low intensity. As the value of $|f|$ decreases, the area of stable regions reduces. At $|f|=0.1$, stable regions, if any, are all too small to locate when $|\rho|$ is not too large such that the system is not in the NLS limit.

For reasons of brevity we show only results for $f=\pm 0.5$ in Figs. 7 and 8. The ratio of the grating strength, γ, is chosen to be 10, 2, and 1 in Figs. 7(a), 7(b), and 7(c), respectively, whereas in Fig. 8 $\gamma=10$ only. Compared to $|f|=1$, the stable regions are much smaller here. The intensity of CW solutions also need to be much lower to be stable. Again, the stable regions shrink as γ decreases. In Fig. 7(a), where $f=-0.5$, and $\gamma=10$, we see a relatively large stable region compared with other cases with similar parameters but smaller γ. This stable region is smaller than that for $f=-1$. We note that the growth rates are modest, making it unlikely that they can be observed in experiments in which the instability grows from noise. In Fig. 8, $f=0.5$, $r_v=1.0$, and $\gamma=10$, and we see that this case still retain some features of Fig. 6(a). The instability growth rate dips at $\rho=0$, resulting in a ''valley.'' However, unlike Fig. 6(a), the valley in Fig. 8 is never deep enough to reach zero. No stable regions are found for $\gamma=2$ and 1.

VI. NUMERICAL SIMULATIONS

To confirm the results of the MI analysis, we also solved the parametric band-gap equations (2.5) numerically. In doing so, we initially take a CW solution inside the grating, with appropriate phase and amplitude to allow a steady-state solution to form, periodic boundary conditions to allow the problem to be treated on a finite domain. If the CW solution is unstable, perturbations grow in time, directly revealing the presence of MI. We used two different numerical schemes: an iterative semi-implicit integration scheme [40] with split-step Fourier transform evaluation of the grating dispersions at the FH and SH, and a method developed originally for gratings with a Kerr nonlinearity [32], but adapted for quadratic nonlinear effect. Both methods' results agree. The first

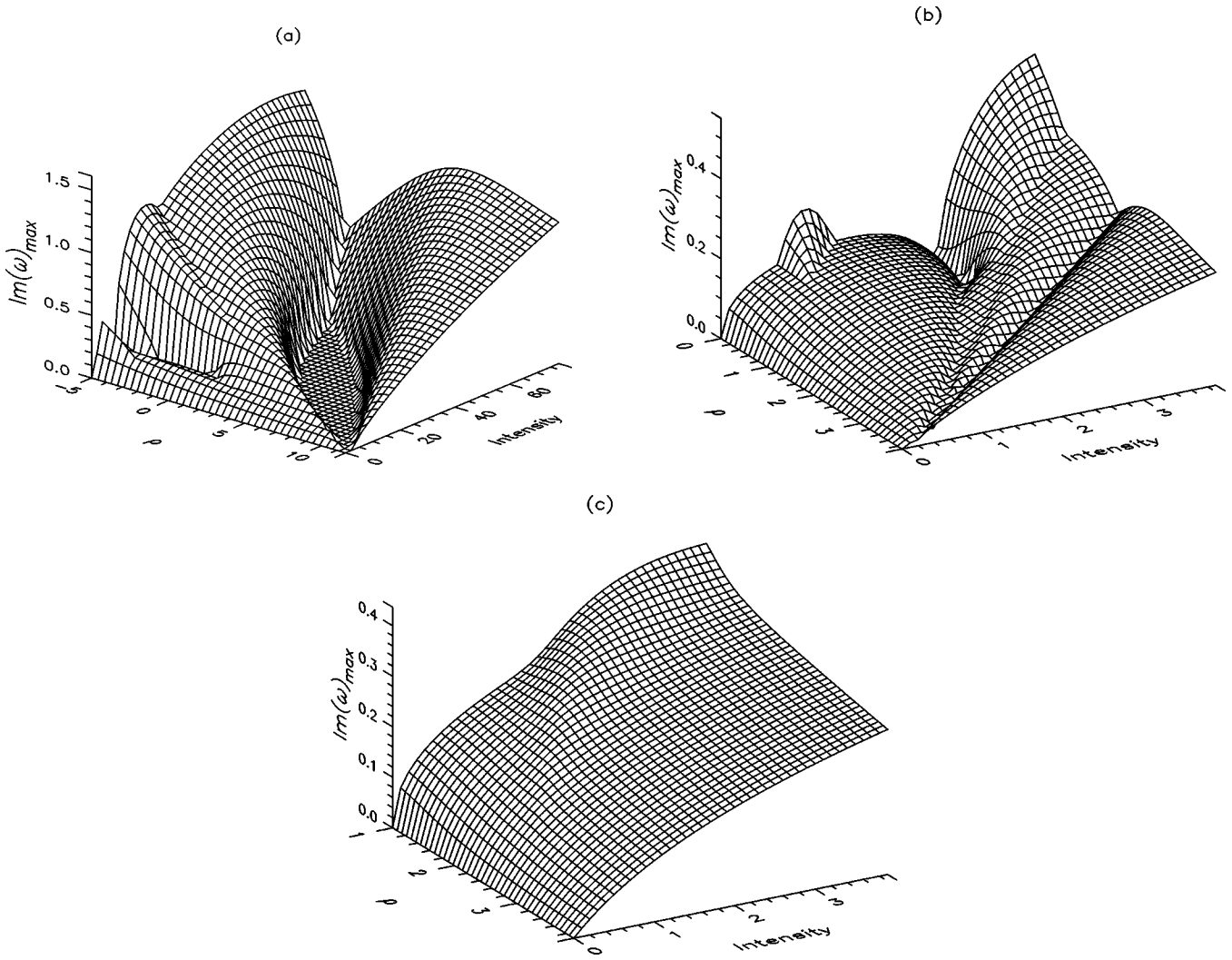

FIG. 6. Maximum instability for different grating strength ratios, γ and positive f. Plotted here is the growth rate vs phase mismatch and intensity. Parameters used are $r_v=1$, $f=1$, (a) $\gamma=10$, (b) $\gamma=2$, and (c) $\gamma=1$. Note that all axes are scaled differently.

method is general and and valid under a wide range of parameters. The second method can only simulate cases with $r_v=1$ but is considerably faster than the first method.

The simulation procedure is as follows: CW solutions are perturbed with Gaussian noises. The noise level is normally 10^{-6}–10^{-7} of the amplitude of the CW solution. These perturbed CW solutions are used as initial conditions. For each set of initial conditions, two independent simulations are performed using the same numerical method. The step size of one simulation is half of that of the other. We compare the results of the two simulations at each time step. When the maximum absolute value of the difference is smaller than 10^{-9}, we accept the simulation results. Otherwise, the step sizes are reduced by half, and simulations are performed again. We note that this procedure is necessary because some cases in which the stability is marginal require a dense numerical grid. Using the above procedures, we propagate each noisy CW solution for an amount of time such that the noise growth is still in the linear region. We then take one mode at two different times and perform a spatial Fourier transform into q, space and filter out the CW component. Finally, we find the ratio of the spectra, and calculate the instability growth rate accordingly. More precisely, we calculate the instability growth rate spectrum using

$$\frac{1}{2}\frac{\ln(|V_{j\pm}(q,\tau_2)|^2)-\ln(|V_{j\pm}(q,\tau_1)|^2)}{\tau_2-\tau_1}. \tag{6.1}$$

The instability growth rate spectrum corresponds to $\mathrm{Im}(\omega(q))$, the largest imaginary part of the eigenvalues. We have simulated a large number of cases. The instability growth rate spectrum is plotted against the theoretical prediction for unstable CW solutions. For example, the evolution of a noisy CW solution is shown in Fig. 9(a). The growth of MI is clearly seen from this figure. The corresponding instability growth rate spectrum is shown in Fig. 9. Dimensionless parameters used for this example are $r_v=1, f=-1, \rho=-1, \gamma=1$, and $\Omega=1.2$. The dotted curve follows from the MI analysis, while the solid curve is obtained from the direct numerical simulation. The curves agree well, confirming the validity of the MI analysis.

Another case worth mentioning is the degenerate CW solutions whose FH components are zero. These solutions generally become stable at low intensities. Such stable degenerate solutions may appear surprising as one might expect that

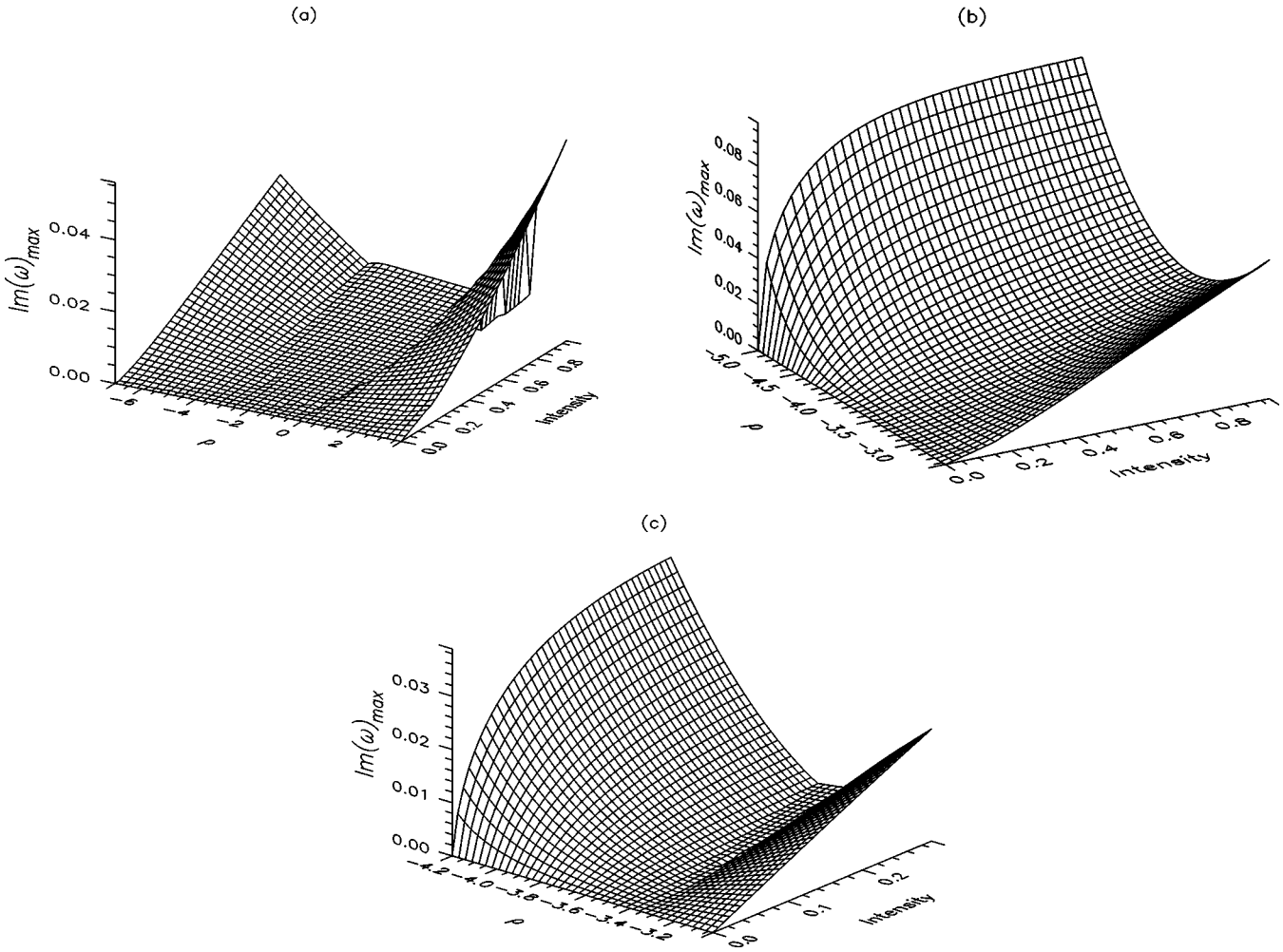

FIG. 7. Maximum instability growth rate versus phase mismatch and intensity for negative f and different grating strength ratios, γ. Parameters used are $f=-0.5$, $r_v=1$, (a) $\gamma=10$; (b) $\gamma=2$ (c) $\gamma=1$.

a single SH photon could lead to down-conversion. However, certain symmetry laws may forbid such down-conversion, and indeed numerical simulations have shown that such stable solutions can propagate for a long time without noise growing. One of such stable cases is $a_{2+}=-a_{2-}=1$, $\gamma=1$, and $r_v=1$. We first take $\rho=4$, so that the stability condition $\Omega^2>a_{2-}^2$ is satisfied. In order to test the stability, the initial CW solution is perturbed with a much stronger Gaussian noise whose amplitude is one percent of that of the CW solution instead of 10^{-6} that we normally use for unstable cases. With a propagating period of 100 and a window size of 20, the noise amplitude remains the same at all time. By contrast, when we take $\rho=0$ and thus the stability condition $\Omega^2>a_{2-}^2$ is not satisfied, the noise amplitude grows quickly even just after a period of 5.

VII. DISCUSSION AND CONCLUSIONS

We have presented a study of MI in a parametric band-gap system. Though this problem reduces to cases that have been studied previously in the NLS limit (see Sec. V A) and the EMA limit (see Sec. V B), the parametric band-gap system is much richer than either of these. Of course this is not unexpected since in both these limiting cases there are one and two relevant modes, respectively, whereas in the most general situation considered here there are four. We note that in the study of MI in a periodic structure with a Kerr nonlinearity [29] it was found that for a range of parameters the solutions were unphysical, in that the MI gain did not vanish as $|q|\to\infty$. It was noted in Ref. [29] that this is likely to be associated with the fact that the dispersion relation of a grating is asymptotically straight. We have observed similar be-

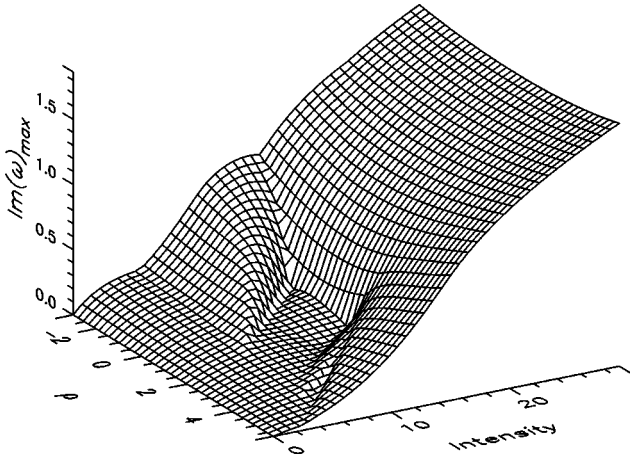

FIG. 8. Maximum instability growth rate vs phase mismatch and intensity for $f=0.5$. Other parameters used are $r_v=1$, and $\gamma=10$.

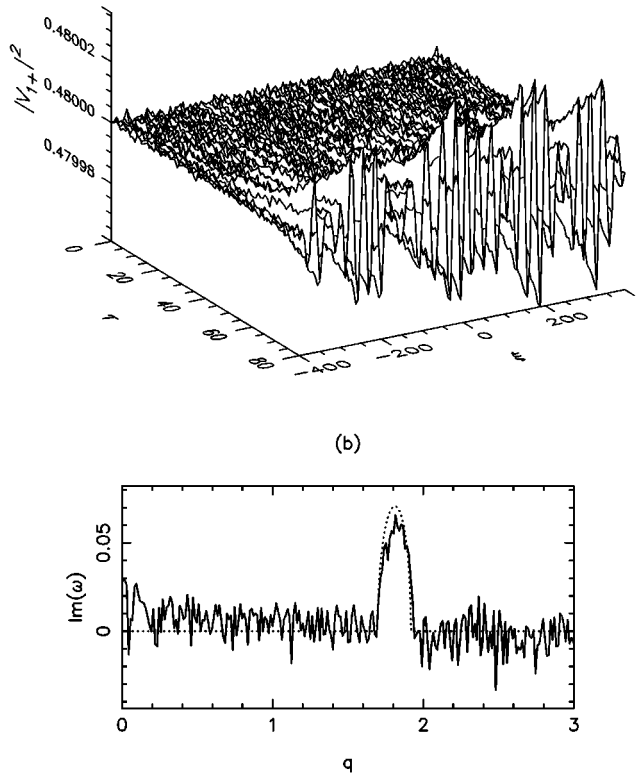

FIG. 9. Numerical demonstration of MI. (a) Evolution of a Gaussian noised CW solution. Shown here is the intensity of the first mode, $|V_{1+}|^2$. (b) Comparison of MI analysis and numerical simulations. Shown here is the instability growth rate vs q, the wave number of noise. The dotted curve is from MI analysis, and the solid curve is from the numerical simulation calculated from Eq. (6.1). Parameters used are $r_v=1$, $f=-1$, $\rho=-1$, $\gamma=1$, and $\Omega=1.2$.

havior in the parametric band-gap system. However, this does not affect the conclusions reached here since, as mentioned in Sec. IV B, only finite values for q are considered.

As mentioned in Sec. IV B, in a large fraction of phase space the CW solutions are unstable. Thus, just like the grating with a Kerr nonlinearity [26], the parametric band gap system could act as a tunable pulse generator. Since in a parametric system the effective nonlinearity can be much larger than that in a Kerr system, the required threshold could be much smaller. Though a detailed consideration of this application is outside the scope of the present work, it is straightforward to obtain a rough estimate for the required intensity. In order to detect the effects of MI in a nonlinear crystal of length l, the time required for a light beam to pass through the crystal should be sufficient for the noise to grow. Since the time required to propagate through the structure is at least l/v_g, we require the instability growth rate to exceed v_g/l. In terms of the the dimensionless units introduced in Eq. (2.4), this can be written as $\mathrm{Im}(\omega)_{\max}>1/(l\kappa_1)$. We take a 1-cm-long $LiNbO_3$ nonlinear crystal as an example and use the following typical values; average refractive index $\bar{n}=2.5$, $\chi^{(2)}=11.9$ pm/V, and input laser wavelength, $\lambda=1.06$ μm. For a grating with 0.2% refractive index modulation, we find that $\kappa_1\approx 1.2\times 10^4$ m^{-1}, and $\chi_E\approx 2.25\times 10^{-5}$ V^{-1}. With these numbers we find $\mathrm{Im}(\omega)_{\max}>0.008$. If $f=1$, $\gamma=1$, $\rho=1$, and $r_v=1$, at an intensity of 0.0012, $\mathrm{Im}(\omega)_{\max}$ has the required value. From Eq. (2.4), the total power required is $P=(\kappa_1/\chi_E)^2\bar{n}^2\epsilon_0 v_g(a_{1+}^2+a_{1-}^2+a_{2-}^2+a_{2+}^2)$ if we take $r_v=1$. We therefore find that $P=0.16$ GW/cm^2 for this case, which is more than an order of magnitude smaller than that required to observe MI in a Kerr system [26].

We also found extended regions of stability, particularly when the SH gap is stronger than that at the FH. Note that this is not the generic situation: for shallow gratings the size of the nth gap is proportional to the magnitude of the nth Fourier component of the refractive index. Since these tend to decrease with increasing n, higher order gaps tend to be smaller than lower order ones. Nonetheless, one can design refractive index profiles in which this is reversed for the two lowest gaps. Though a detailed analysis of dark solutions outside the scope of this paper, one may conclude that in such systems the stability of dark soliton solutions is not ruled out by an unstable background. It is interesting that the full problem needs to be analyzed to reach this conclusion, as the EMA approximation fails if $|q|$ is too large.

The key restriction to our work is that we assume type I phase matching, in which the FH is linearly polarized. Though, in principle, it would be straightforward to generalize to type II phase matching, in which the FH consists of two distinct linearly polarized components, in practice it would be complicated. First of all, Eqs. (2.3) would be replaced by six coupled equations, rather than four, leading to the need to evaluate a 12×12 matrix, rather than the 8×8 matrix (4.11). Moreover, the available phase space would be much larger, making global searches of the solutions increasingly time-consuming.

In conclusion, we studied MI in a type I phase matched parametric band-gap system. We find the expected behavior in the NLS limit. We have not studied the EMA approximation in detail here, because even though the EMA approximation can apply to the CW solution, the instabilities may be too rapidly varying for the EMA to hold. Indeed, the results are dominated by the existence of large regions of modulational instability, which could find applications in low intensity short-pulse generation. In spite of this, the work presented here also shows substantial stable regions for some parameter values, in which steady-state solutions can occur. In these regions, the existence of dark soliton solutions is not ruled out.

ACKNOWLEDGMENTS

B.A.M. acknowledges support from the University of New South Wales. The authors thank Iver Cairns for a useful discussion. M. H. acknowledges support from the Australian Research Council.

APPENDIX A: GENERAL CW SOLUTIONS

In this section, we consider general nondegenerate CW solutions. Moving $a_{1\pm}$ to the right side of Eq. (3.2) and dividing them, together with the expression of $a_{2\pm}$, we arrive at

$$\frac{(2\Omega+2r_vQ+\rho)(-f^{-1}-Q-\Omega)+\gamma(-f+Q-\Omega)}{(2\Omega-2r_vQ+\rho)(-f+Q-\Omega)+\gamma(-f^{-1}-Q-\Omega)}=f^2, \tag{A1}$$

which does not depend on a. Let Ω and f be the free parameters, one can then solve the above equation for Q. Rearranging, we obtain a quadratic equation for Q:

$$AQ^2+BQ+C=0 \tag{A2}$$

where

$$A=2r_v(f^2-1),$$

$$B=\frac{f(1+f^2)(\gamma-\rho-2\Omega)-2r_v(1+f^4+f\Omega+f^3\Omega)}{f},$$

$$C=\frac{(-1+f^2)[\rho(1+f^2+f\Omega)+\Omega(2+2f^2+f(\gamma+2\Omega))]}{f} \tag{A3}$$

Once Q has been determined from Eq. (A2), adding Eqs. (3.2) gives an equation for a, which reads,

$$a^2=(2\Omega+\rho+\gamma)(f+f^{-1}+2\Omega)+2r_vQ(-f+f^{-1}+2Q). \tag{A4}$$

For a given set of f and Ω, one can work out Q by solving Eq. (A2); both solutions for Q need to be considered. Substituting Q into Eq. (A4), one obtains a. CW solutions can be found subsequently from Eqs. (3.5) and (3.6) .

APPENDIX B: PARAMETRIC EQUATIONS

The parametric equation first appeared in Ref. [1]. It has been extensively studied recently [3–16]. Based on the published model [4], we rewrite the one-dimensional parametric equation describing the cascaded $\chi^{(2)}$ parametric waveguide in the forms

$$\left(\frac{\partial}{\partial z}+\frac{ik_1''}{2}\frac{\partial^2}{\partial t^2}\right)\phi_1=i\chi\phi_2\phi_1^*, \tag{B1a}$$

$$\left(\frac{\partial}{\partial z}+\frac{ik_2''}{2}\frac{\partial^2}{\partial t^2}-i\beta\right)\phi_2=\frac{i\chi}{2}\phi_1^2, \tag{B1b}$$

where k_j'' is the dispersion at the jth frequency, i.e., the derivative $d^2k/d\omega^2$ calculated at the point $k=k_j$. Here $\beta=k_0^{(2)}-2k_0^{(1)}$ where $k_0^{(1)}$ and $k_0^{(2)}$ are wave numbers of the first and second harmonics, while the nonlinearity χ is given as

$$\chi=\frac{\epsilon_0\chi^{(2)}k_0^{(1)}}{\epsilon_1}\left(\frac{\hbar k_0^{(2)}}{2\epsilon_2}\right)^{1/2}\int d^2x(u^{(1)}(x))^2(u^{(2)}(x))^*, \tag{B2}$$

where $u^{(j)}(x)$ refers to normalized transverse-mode functions. The fields ϕ_1 and ϕ_2 are, respectively, the complex envelopes of the first and second harmonics, in units defined so that $|\phi_j|^2$ is the photon flux of the jth field. In this equation, it is assumed that the group velocities $v_j=d\omega/dk$ of the two fields match at the carrier frequency, to optimize simulton formation. Under the EMA, the parametric band-gap equation (2.3) can be approximated by Eq. (B1), with the parameters taking different definitions [22,23].

[1] Y. N. Karamzin and A. P. Sukhorukov, Pis'ma Zh. Eksp. Teor. Fiz. **20**, 734 (1974) [JETP Lett. **20**, 339 (1974)].
[2] Y. N. Karamzin and A. P. Sukhorukov, Zh. Éksp. Teor. Fiz. **68**, 834 (1975) [Sov. Phys. JETP **41**, 414 (1976)].
[3] S. Trillo, M. Haelterman, and A. Sheppard, Opt. Lett. **22**, 970 (1997).
[4] M. J. Werner and P. D. Drummond, J. Opt. Soc. Am. B **10**, 2390 (1993).
[5] M. A. Karpierz and M. Sypek, Opt. Commun. **110**, 75 (1994).
[6] C. R. Menyuk, R. Schiek, and L. Torner, J. Opt. Soc. Am. B **11**, 2434 (1994).
[7] K. Hayata and M. Koshiba, Phys. Rev. A **50**, 675 (1994).
[8] A. V. Buryak and Y. S. Kivshar, Opt. Lett. **19**, 1612 (1994).
[9] L. Torner, C. R. Menyuk, and G. I. Stegeman, J. Opt. Soc. Am. B **12**, 889 (1995).
[10] L. Torner, Opt. Commun. **114**, 136 (1995).
[11] L. Torner, C. R. Menyuk, and G. I. Stegeman, Opt. Lett. **19**, 1615 (1994).
[12] A. V. Buryak and Y. S. Kivshar, Phys. Rev. A **51**, R41 (1995).
[13] H. He, M. Werner, and P. D. Drummond, Phys. Rev. E **54**, 896 (1996).
[14] A. V. Buryak and Y. S. Kivshar, Opt. Lett. **20**, 834 (1995).
[15] A. V. Buryak, Y. S. Kivshar, and V. V. Steblina, Phys. Rev. A **52**, 1670 (1995).
[16] A. V. Buryak and Y. S. Kivshar, Phys. Lett. A **197**, 407(1995).
[17] P. D. Drummond and H. He, Phys. Rev. A **56**, R1107 (1997).

[18] P. D. Drummond and H. He (unpublished).
[19] W. E. Torruellas, Z. Wang, D. J. Hagan, E. W. Vanstryland, G. L. Stegeman, L. Torner, and C. R. Menyuk, Phys. Rev. Lett. **74**, 5036 (1995).
[20] P. D. Trapani, D. Caironi, G. Valiulis, A. Dubietis, R. Danielius, and A. Piskarskas, Phys. Rev. Lett. **81**, 570 (1998).
[21] B. J. Eggleton, R. E. Slusher, C. M. de Sterke, P. A. King, and J. E. Sipe, Phys. Rev. Lett. **76**, 1627 (1996).
[22] H. He and P. D. Drummond, Phys. Rev. E **58**, 5025 (1998).
[23] H. He and P. D. Drummond, Phys. Rev. Lett. **78**, 4311 (1997).
[24] T. Peschel, U. Peschel, F. Lederer, and B. A. Malomed, Phys. Rev. E **55**, 4730 (1997).
[25] C. Conti, S. Trillo, and G. Assanto, Phys. Rev. Lett. **78**, 2341 (1997); Phys. Rev. E **57**, R1251 (1998); Opt. Lett. **23**, 334 (1998).
[26] B. J. Eggleton, C. M. de Sterke, R. Slusher, and J. Sipe, Electron. Lett. **32**, 2341 (1996).
[27] S. Trillo and P. Ferro, Opt. Lett. **20**, 438 (1995).
[28] H. He, P. D. Drummond, and B. A. Malomed, Opt. Commun. **123**, 395 (1996).
[29] C. M. de Sterke, J. Opt. Soc. Am. B **15**, 2660 (1998).
[30] A. B. Aceves, C. De Angelis, and S. Wabnitz, Opt. Lett. **17**, 1566 (1992); H. G. Winful, R. Zamir, and S. Feldman, Appl. Phys. Lett. **58**, 1001 (1991); B. J. Eggleton, C. M. de Sterke, A. B. Aceres, J. E. Sipe, T. A. Strasser, and R. E. Slusher, Opt. Commun. **149**, 267 (1998).
[31] P. D. Drummond, Comput. Phys. Commun. **29**, 211 (1983).
[32] C. M. de Sterke, K. R. Jackson, and B. D. Robert, J. Opt. Soc. Am. B **8**, 403 (1991).
[33] E. M. Dianov, V. P. Konyaev, and Yu. V. Kurnyavko, Zh. Tekh. Fiz. **16**, 48 (1990) [Sov. Tech. Phys. Lett. **16**, 866 (1990)]; Sov. J. Quantum Electron. **21**, 360 (1991); W. P. Risk and S. D. Lau, Opt. Lett. **18**, 272 (1993); W. P. Risk, S. D. Lau, and M. A. McCord, IEEE Photonics Technol. Lett. **6**, 406 (1994).
[34] P. D. Drummond, K. J. McNeil, and D. F. Walls, Opt. Acta **28**, 211 (1981).
[35] See, for example, J. Opt. Soc. Am B **10** (1993), edited by L. Hesselink, E. Kratzig, and K. H. Ringhofer.
[36] A. Arraf and C. M. de Sterke, Phys. Rev. E **58**, 7951 (1998).
[37] G. P. Agrawal, *Nonlinear Fiber Optics*, 2nd ed. (Academic, San Diego, 1995).
[38] C. Conti, S. Trillo, and G. Assanto, Opt. Lett. **23**, 1265 (1998).
[39] C. Conti, S. Trillo, and G. Assanto, Opt. Lett. **22**, 1350 (1997).
[40] P. D. Drummond and I. K. Mortimer, J. Comput. Phys. **93**, 144 (1991).